

Eruption Forecasting of Strokkur Geyser, Iceland, Using Permutation Entropy

Maria R.P. Sudibyo¹, Eva P.S. Eibl¹, Sebastian Hainzl², Gylfi Páll Hersir^{3,4}

¹University of Potsdam, Institute for Geosciences, Karl-Liebknecht-Str.24/25, Potsdam-Golm

²GFZ German Research Centre for Geosciences, Telegrafenberg, 14473 Potsdam, Germany

³ISOR, Iceland GeoSurvey, Urdarhvarf 8, Reykjavik, Iceland

⁴Presently gylfi.pall@outlook.com

Key Points:

- Permutation Entropy (PE) is a simple tool to assess the complexity of a time series.
- We analyzed the PE evolution for 63 eruptive cycles of Strokkur geyser and found characteristic changes in PE during recharge.
- PE is found to be a useful statistical predictor of the eruption times and highlights the precursor 15 s before eruptions.

Corresponding author: Maria R.P. Sudibyo, pujiastutisudibyo@uni-potsdam.de

Abstract

A volcanic eruption is usually preceded by seismic precursors, but their interpretation and use for forecasting the eruption onset time remain a challenge. A part of the eruptive processes in open conduits of volcanoes may be similar to those encountered in geysers. Since geysers erupt more often, they are useful sites for testing new forecasting methods. We tested the application of Permutation Entropy (PE) as a robust method to assess the complexity in seismic recordings of the Strokkur geyser, Iceland. Strokkur features several minute-long eruptive cycles, enabling us to verify in 63 recorded cycles whether PE behaves consistently from one eruption to the next one. We performed synthetic tests to understand the effect of different parameter settings in the PE calculation. Our application to Strokkur shows a distinct, repeating PE pattern consistent with previously identified phases in the eruptive cycle. We find a systematic increase in PE within the last 15 s before the eruption, indicating that an eruption will occur. We quantified the predictive power of PE, showing that PE performs better than seismic signal strength or quiescence when it comes to forecasting eruptions.

Plain Language Summary

When a volcano shows the first sign of activity, it is challenging to determine whether and when the actual eruption will occur. Usually, researchers create earthquake lists and locate these events to assess this. However, an alternative and simpler method can be directly applied to continuous seismic data. We tested a method that assesses the complexity of signals. We first created synthetic data to find reasonable parameter settings for this method. While volcanoes do not erupt very often, frequent eruptions at geysers allow us to systematically study and compare several eruptions. We analyzed the continuous record of 63 eruptions of the Strokkur geyser, Iceland. Our results show a distinct pattern that repeats from one eruption to the next one. We also find a clear pattern that indicates about 15 s before the next eruption that an eruption will occur. We show that this method performs better in eruption forecasting than assessing the seismic noise or silence caused by the geyser.

1 Introduction

When a volcano becomes restless, it is challenging to assess whether it will lead to an actual eruption and determine the timing of the eruption onset. A magmatic intrusion starting at depth can (i) remain at depth, (ii) stall just before reaching the surface, (iii) erupt in sluggish and viscous extrusion, or (iv) erupt rapidly or explosively (Moran et al., 2011). The process of magma migration involves interactions with the surrounding country rock, cooling magma bodies from previous eruptions, and (or) hydrothermal system (Moran et al., 2008). These interactions generate natural phenomena such as earthquakes, deformation, temperature changes, and gas emissions. These phenomena can be observed by geophysical and geochemical measurements (Moran et al., 2008) and integrated with the history of past eruptions in a framework of eruption forecasting (Whitehead & Bebbington, 2021).

From a seismic point of view, eruptions can show precursors such as accelerating or decelerating earthquake rates. To assess this, monitoring institutes conventionally use methods to tabulate daily event counts (McNutt, 1996) and calculate the average amplitude for a certain window length (Endo & Murray, 1991). The Failure Forecast Method estimates the onset time of eruption by using the rate and the acceleration of seismic precursors associated with the rock failure caused by magma propagation (Boué et al., 2015). However, this method cannot deal with complex precursory signals, e.g., that exhibits fluctuations or deceleration (Boué et al., 2015). Furthermore, due to the uncertainty of the eruption forecast and numerous false alarms (Bell et al., 2013), this method is not recommended to be stand-alone (Whitehead & Bebbington, 2021). Dempsey et al. (2020)

65 tested a real-time Machine Learning framework to detect eruption precursors of five ma-
 66 jor eruptions at Whakaari volcano, New Zealand, from 2011 to 2020. This framework
 67 derives the information from the seismic amplitude between different frequency bands
 68 to assess whether an eruption will occur. A challenge lies in the threshold determina-
 69 tion: while increasing the threshold will eliminate false predictions, it leads to missing
 70 eruptions and vice versa.

71 Permutation Entropy, referred to as PE, quantifies the complexity of time series
 72 in a simple way, allowing us to characterize the evolution of a dynamic system (Bandt
 73 & Pompe, 2002). The calculation of PE relies on the number of permutations appear-
 74 ing in a data series, also known as ordinal pattern, which has been proved to be sensi-
 75 tive in detecting dynamical changes (Cánovas et al., 2011; Cao et al., 2004). PE is widely
 76 applied in biomedical science, such as epilepsy detection and prediction, discriminating
 77 depth level of anesthesia, and distinguishing heart rate to assess the possibility of heart
 78 failure, as has been summarized by Zanin et al. (2012). Although the original algorithm
 79 of PE is robust, efforts in PE modification have been made to improve its capability in
 80 handling structural changes in different data types. Examples are Tsallis Permutation
 81 Entropy to improve the characterization of different stochastic processes (Zunino et al.,
 82 2008) and Rényi Permutation Entropy, which uses Rényi Entropy (Rényi, 1960) in the
 83 calculation of PE, in order to distinguish rare from frequent events (Zhao et al., 2013).
 84 The PE modifications are not only limited to the amplitude information but also concern
 85 the signal’s phase information, as recently proposed by Kang et al. (2021) as Phase
 86 Permutation Entropy.

87 A robust forecasting framework requires incorporating different forecasting attributes
 88 from multiple methods. Testing the application of new methods is important to improve
 89 the reliability of the forecasting framework. Glynn and Konstantinou (2016) successfully
 90 used the original PE algorithm to detect precursors prior to the 1996 Gjálp eruption. This
 91 motivates us to further assess PE’s capability and limitation in detecting dynamical changes
 92 prior to eruptions.

93 Geysers are hot springs characterized by intermittent discharge of water that erupts
 94 turbulently and is accompanied by a vapor phase (White, 1967). The eruption process
 95 of geysers requires magmatism as a heat source, abundant water recharge, and a plumb-
 96 ing system (Hurwitz & Manga, 2017). While the type of liquid and gas phase in geysers
 97 differs from the liquid, gas, and solid phase in magma, the fluid is driven to eruption by
 98 the gases in both cases. Therefore, the knowledge gained from understanding geyser erup-
 99 tions might provide useful insights for monitoring volcanic eruptions.

100 Here, we tested the application of PE for forecasting eruptions at Strokkur geyser,
 101 Iceland (Fig. 1a and b). The Strokkur geyser is an ideal site for three reasons: (1) Strokkur
 102 features a several-minute long eruptive cycle (Eibl et al., 2021) which allows us to check
 103 if PE behaves consistently from one cycle to the next one, (2) the features of the erup-
 104 tive cycle were already described and interpreted multidisciplinary (Eibl et al., 2021)
 105 and provide a benchmark for our study, (3) the available instrument network (Fig. 1b)
 106 consists of seismometers located at a few meter distance from the geyser’s conduit, pro-
 107 viding signals with a high signal-to-noise ratio, and seismometers installed at 38.3 to 47.3 m
 108 distance, providing a good configuration to test the sensitivity of PE towards station dis-
 109 tance.

110 In this publication, we first introduce the PE method (section 2.1) and perform sev-
 111 eral synthetic tests to choose the optimum parameters for PE calculations (section 2.2).
 112 We also introduce the Receiver Operating Characteristic (ROC) analysis (section 2.3)
 113 to assess the predictive power of PE. Then, the methods are applied to eruptions of the
 114 Strokkur geyser (section 3 and 4). We compare PE with seismic root-mean-square val-
 115 ues (RMS) for one eruptive cycle (section 5.1) and stacked for all available single erup-
 116 tive cycles (section 5.2). We assess PE for other eruption types (section 5.3) and the change

117 of PE with distance (section 5.4). We discuss how PE relates to the seismic sources mi-
 118 gration (section 6.1), the influence of source strength and path effects toward PE(section
 119 6.2) and its predictive power for eruptions at the Strokkur geyser (section 6.3). We con-
 120 clude that PE detects a clear precursory signal at stations at a few meter distance, making
 it a promising tool in eruption forecasting.

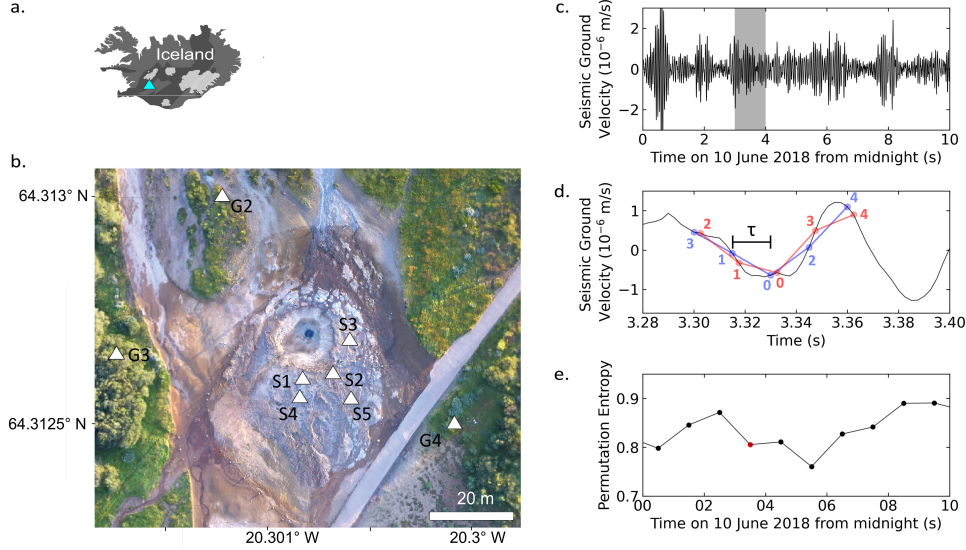


Figure 1. Overview of seismic network near Strokkur geyser, Iceland and the calculation of PE. (a) Location of the Strokkur geyser in Iceland (blue triangle) and (b) aerial map where white triangles indicate the location of the seismometers (7L network). (c) 10 s seismogram recorded by the vertical component of station S1. The seismogram is divided into 10 bins of 1 s. The shaded part is related to one of those bins. (d) A closer view of 0.12 s seismic data taken from the shaded window in subfigure (c). The blue and red dot-connecting-lines visualize two consecutive ordinal patterns, $\{3, 1, 0, 2, 4\}$ and $\{2, 1, 0, 3, 4\}$ respectively. Each pattern is constructed from five consecutive values selected using $m = 5$ and $\tau = 0.0015$ s. The length of τ is visualized as a black horizontal scalebar. (e) The 10 PE values calculated for the consecutive 1 s time window in subfigure (c), where the red dot refers to the PE calculated for the shaded time window in subfigure (c).

121

122 2 Methods and Synthetic Test

123 2.1 Calculation of Permutation Entropy (PE)

124 Permutation Entropy is a robust way to quantify the complexity of a time series
 125 (Bandt & Pompe, 2002; Zanin et al., 2012; Riedl et al., 2013). This PE method analyzes
 126 the probability distribution of ordinal patterns observed in the data (Bandt & Pompe,
 127 2002). An ordinal pattern is a vector representing the relative order of amplitude of the
 128 successive samples in a sequence of time series (Bandt & Pompe, 2002; Zanin et al., 2012;
 129 Riedl et al., 2013). For example, a sequence of $\{0.5, 1.0, 3.5, 4.0, 5.7\}$, based on their am-

130 plitude order, is represented as an ordinal pattern of $\{0, 1, 2, 3, 4\}$ and a sequence of $\{1.1,$
 131 $0.8, 0.7, 1.3, 1.0\}$ is represented as an ordinal pattern of $\{3, 1, 0, 4, 2\}$.

132 To construct an ordinal pattern, we basically downsample the time series using an
 133 embedding dimension and a delay time. The embedding dimension is the number of sam-
 134 ples used to construct an ordinal pattern, i.e., the length of the ordinal pattern, while
 135 the delay time is the time gap between the successive samples constructing the ordinal
 136 pattern. The ordinal pattern is then defined by a vector of $x_s, x_{s+\tau}, \dots, x_{s+(m-1)\tau}$, where
 137 x_s is the first sample in the sequence, m is the embedding dimension and τ is the de-
 138 lay time (Zanin et al., 2012; Riedl et al., 2013). If equal values of amplitude are selected,
 139 these values are ranked based on their temporal order (Zumino et al., 2017). To extract
 140 all ordinal patterns in a short time window, we continuously shift x_s one sample forward
 141 until the last ordinal pattern reaches the end of the window. The PE for the time bin
 142 is then calculated as follows:

$$143 \quad PE = \frac{-1}{\log m!} \sum_{k=1}^{m!} p_k \log p_k \quad (1)$$

144 where p_k is the probability of the ordinal pattern k , and m is the value of the embed-
 145 ding dimension. p_k is estimated by the relative frequency N_k/N , where N_k represents
 146 the number of recurrences of pattern k and N is the total number of ordinal patterns
 147 observed in the time window. The maximum number of different ordinal patterns in a
 148 time series signal is $m!$. Equation (1) is normalized with $\log(m!)$ to limit the value of PE
 149 to the range of 0 to 1. We then repeat the PE calculation for the next time bin that does
 150 not overlap with the previous one until the whole time period of interest is processed,
 151 and we can study the PE changes in time.

152 An example of PE calculated for seismic data of station S1 at Strokur (see Fig. 1b)
 153 is illustrated in Fig. 1c-e. Here, we first divided the seismic time series into 1 s-windows
 154 (Fig. 1c), in which the ordinal patterns were extracted using $m = 5$ and $\tau = 0.015$ s
 155 (Fig. 1d). We define the delay time as the time gap in seconds as we deal with seismic
 156 time series that were recorded with different sampling rates. In each 1 s-window, we then
 157 estimated the probability distribution of the ordinal patterns and calculated the respec-
 158 tive PE value (Fig. 1e).

159 2.2 Synthetic Test of Permutation Entropy

160 The calculation of PE requires the choice of the delay time, embedding dimension,
 161 and the length of time bins (e.g., the shaded window in Fig. 1c). We created several syn-
 162 thetic signals with and without noise to explore the role of these parameters and to de-
 163 fine reasonable settings for the PE calculation. The synthetic signals were generated us-
 164 ing the basic formula $x(t) = \sin(2\pi ft)$ and a sampling rate of 100 Hz. We set the length
 165 of the signals to 20000 s. For all tests, we used delay times τ ranging from $0.01T_0$ to T_0
 166 with a step size of $0.01T_0$, where $T_0 = 1/f$ is the fundamental period of the signal, and
 167 embedding dimensions m range from 3 to 9. Since one point cannot create any vectors,
 168 and two points can only construct a vector with two possible directions, up and down,
 169 $m = 3$ becomes the smallest embedding dimension to assemble ordinal patterns (Zanin
 170 et al., 2012). In this test, $m = 9$ was chosen as the upper limit due to the high com-
 171 putational cost. To find out whether the wavelength of the targeted signal should be con-
 172 sidered when choosing the window length, we tested 8 different monochromatic signals
 173 with different wavelengths. All synthetic tests were performed using Python (Van Rossum
 174 & Drake, 2009).

175 We first tested a pure monochromatic signal with $f = 1$ Hz (Fig. 2a) to evalu-
 176 ate the effect of different delay times and embedding dimensions. We observed that the
 177 minimum PE is obtained when the shortest delay time, i.e. $\tau = 0.01$ s, and a delay time
 178 τ close to T_0 was used (Fig. 2c). We expected that the minimum PE is obtained when

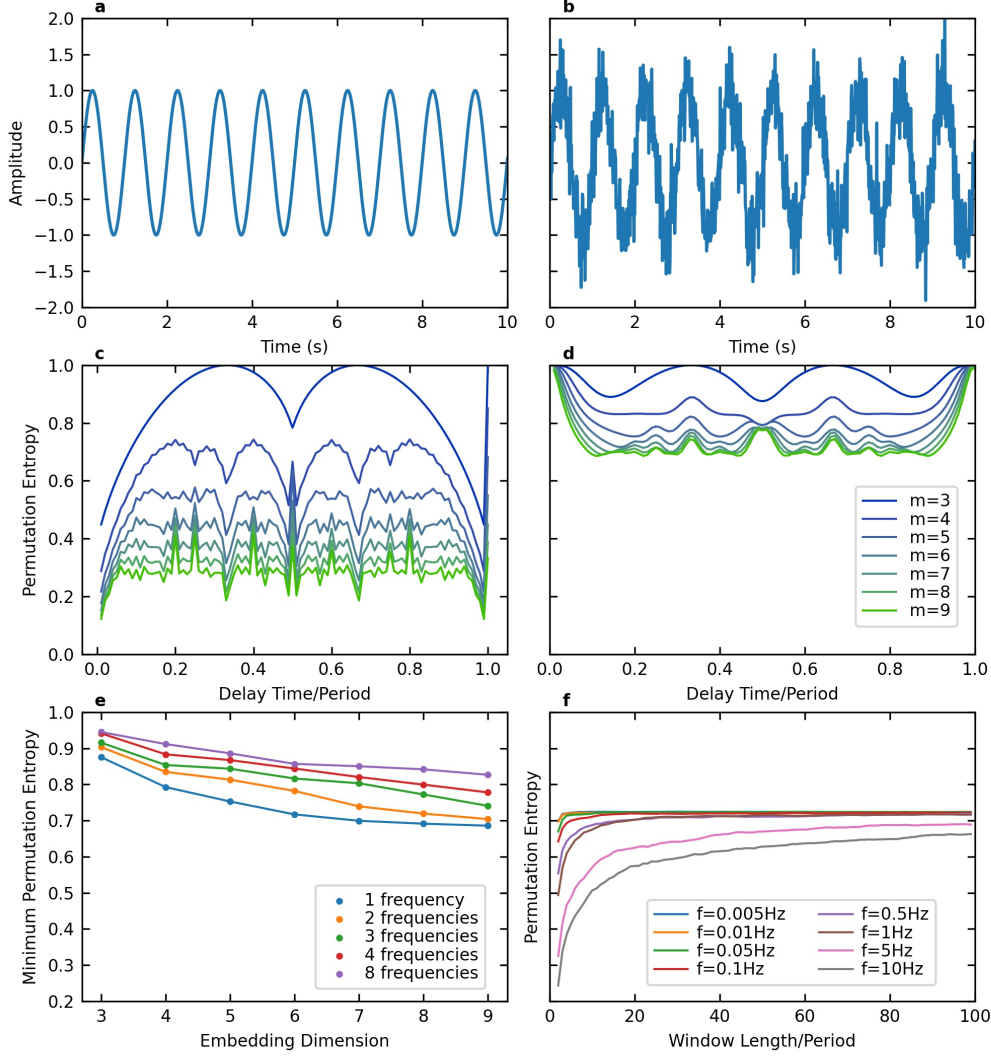


Figure 2. Synthetic test for PE calculation. 10 s zoom of the 2000 s synthetic signal with a frequency of $f=1$ Hz (a) without noise, (b) with $\text{SNR}=5$, (c) PE calculated from the signal in subfigure (a) using embedding dimensions m from 3 to 9 and delay times τ from $0.01 T_0$ to T_0 with step size $0.01 T_0$. $T_0=1/f$ is the period of the signal. (d) Same as subfigure (c) for the signal in subfigure (b), (e) Minimum PE values for 5 synthetic signals, with different complexity and $\text{SNR}=5$, calculated using the same embedding dimensions and delay times as in subfigure (c), (f) PE calculated for 8 different monochromatic signals with frequencies f between 0.005 and 10 Hz using $m=7$ and $\tau=0.2/f$. The synthetic signals used for subfigures (e) and (f) are shown in Fig. S1.

179 using $\tau = T_0$, since the delay time will select equal values of amplitude and construct
 180 a repeated ordinal pattern through the window. However, we obtained a very high PE,
 181 close to 1 (Fig. 2c) for $\tau = T_0$. After checking the synthetic sine wave constructed using
 182 the numpy library (Harris et al., 2020), we found that there are small differences in
 183 the order of $10^{(-16)}$ between the amplitudes of the same wave phase, due to the floating-

184 point error. While the relative differences between values are negligible, the tiny differ-
 185 ences disturb the ranking and create random ordinal patterns, resulting in PE close to
 186 1.

187 To make the time series more complex, in the next step, we (i) added noise to the
 188 signal and (ii) added different frequencies to create different signal types. We quantified
 189 the noise level by the signal-to-noise ratio (SNR), defined as the ratio between the vari-
 190 ance of signal and noise. The SNR hence can be calculated according to

$$191 \quad SNR = \frac{\sigma_S^2}{\sigma_N^2} \quad (2)$$

192 where σ_S is the standard deviation of the signal and σ_N is the standard deviation of the
 193 noise. We used SNR=5 to create noise and added it to the monochromatic signal (Fig. 2b).
 194 The analysis of the synthetic signal shows that PE is equal to 1 when calculated using
 195 the shortest delay time and delay time equal to T_0 (Fig. 2d). We infer that the delay time
 196 should not be short nor equal to the fundamental period.

197 In the next step, we generated four different signals containing two, three, four, and
 198 eight frequencies, with and without noise (see Fig. S1 for the detailed information on the
 199 frequency content). The PE was calculated using the same delay time and embedding
 200 dimension as for the monochromatic signal. The result shows higher PE obtained for the
 201 signal containing more frequencies (Fig. 2e and Fig. S1). Similar to the monochromatic
 202 signal without noise, the minimum PE is obtained using $\tau = 0.001$ s and τ close to T_0 ,
 203 while the signals with noise reach PE close to 1 when using $\tau = 0.001$ s and τ close to
 204 T_0 .

205 According to the PE result in Fig. 2c and d, and Fig. S1, using a higher embed-
 206 ding dimension will result in a lower PE. To see how the PE changes, we plotted the min-
 207 imum PE for the monochromatic signal (Fig. 2b) and four different signals in Fig. S1 with
 208 SNR=5 in Fig. 2e. The minimum PE is obtained for each embedding dimension, calcu-
 209 lated from different delay times ranging from $0.01T_0$ to T_0 . PE generally converges for
 210 each signal, meaning that PE decreases less when using higher embedding dimensions.

211 Another requirement for PE calculation is that the window length has to accom-
 212 modate the maximum number of possible ordinal patterns. Additionally, we need to con-
 213 sider the dominant period of the targeted signal. We tested eight different monochro-
 214 matic signals, with the frequencies f ranging from 0.005 Hz to 10 Hz (see Fig. 2d for the
 215 detailed list of frequencies) with SNR=5 and a sampling frequency of 100 Hz. PE was
 216 calculated using $m = 7$ and $\tau = 0.2T_0$ (see Fig. 2d). The delay time $\tau = 0.2T_0$ was
 217 chosen based on the result in Fig. 2f, where PE is minimum using $\tau = 0.2T_0$. The max-
 218 imum possible number of different ordinal patterns related to the embedding dimension
 219 of 7 is 7! or 5040 ordinal patterns. The PE calculated for the signals with low frequen-
 220 cies, e.g. 0.005 Hz and 0.01 Hz, are stable when the window length is $3 T_0$. In this case,
 221 the signal is much longer than required by $m = 7$. However, the number of points within
 222 $3 T_0$ reduces with increasing signal frequencies given the fixed sampling frequency. There-
 223 fore, the signals with frequencies higher than 1 Hz require more than $3 T_0$ to contain enough
 224 samples required by the embedding dimension. In conclusion, the window length should
 225 provide enough points for the embedding dimension and be longer than the targeted sig-
 226 nal period.

227 **2.3 Receiver Operating Characteristic (ROC) Analysis**

228 A well-known method to analyze the ability to predict an event, such as earthquakes
 229 or volcanic eruptions (DeVries et al., 2018; Spampinato et al., 2019), is the receiver op-
 230 erating characteristic (ROC) analysis (Fawcett, 2006). ROC analyzes the value of the
 231 predictor variable relative to a threshold. Four possible outcomes are possible: If the vari-
 232 able exceeds the threshold and an event (i.e., eruption in our case) follows within the alarm

233 period (the subsequent N_T time steps), it is a hit (true positive, TP); otherwise, it is a
 234 false alarm (false positive, FP). If no alarm is raised because the variable is below the
 235 threshold, either no event might occur (true negative, TN), or an event occurs (false neg-
 236 ative, FN) within the next N_T time steps. In this way, each value of the time series is
 237 associated with one of the values TP, FP, TN, or FN, and their counts are calculated
 238 for the whole time series. Based on these counts, the true positive rate $\text{TPR} = \text{TP} / (\text{TP}$
 239 $+ \text{FN})$ and the false positive rate $\text{FPR} = \text{FP} / (\text{TN} + \text{FP})$ are determined. The ROC
 240 curve is finally created by plotting TPR against FPR for threshold values ranging from
 241 the minimum to the maximum value of the assessed variable (here, RMS or PE). Both
 242 TPR and FPR range between 0 and 1. For quantification, the area under the TPR curve
 243 (AUC) is calculated for FPR ranging from 0 to 1. An optimal predictor variable has $\text{AUC}=1$,
 244 while the ROC curve of a random variable scatters around the diagonal with $\text{AUC}\approx 0.5$.
 245 We applied this method to our PE and RMS time series, using a time window of 1 s to
 246 predict an eruption in the following 1 s window.

247 **3 Overview of Instrument Network near Strokkur and Eruption Be-** 248 **haviour of Strokkur**

249 Strokkur geyser is a part of the Geysir geothermal area in the Haukadalur valley
 250 in southwest Iceland (Fig. 1). On the surface, Strokkur hosts a water-filled pool of 12 m
 251 in diameter (Rinehart, 1986). In the middle of the pool, the uppermost part of the sin-
 252 ter conduit walls extends to the surface (Eibl et al., 2021). This conduit is 2.2 m wide
 253 and changes shape and width with depth (Walter et al., 2020). Strokkur features sin-
 254 gles to sextuple eruptions with one to six water fountains jetting into the air with an av-
 255 erage interval of 16.1 s between fountains (Eibl, Hainzl, et al., 2020). Within this manuscript,
 256 we only assessed single to quadruple eruptions for which the waiting time after eruptions
 257 increases linearly from 3.7 ± 0.9 minutes to 11.3 ± 2.9 minutes (Eibl, Hainzl, et al., 2020).

258 We used seismic data recorded at 5 to 14 m distance south and east of the pool of
 259 Strokkur geyser, Iceland (Eibl, Walter, et al., 2020). The sensors are Nanometrics Tril-
 260 lium Compact Posthole 20 s seismometers at locations S2, S3, S5 and Nanometrics Tril-
 261 lium Compact 120 s at locations S1, S4 (see Fig. 1b) in the 7L seismic network (Eibl,
 262 Walter, et al., 2020). The seismometers were installed on 10 June 2018 for 4.5 to 5.25
 263 hours and recorded at a sampling rate of 400 Hz. To assess the sensitivity of PE with
 264 respect to station distance from the source, we utilized the seismic data recorded at sta-
 265 tions G2, G3, and G4 at a distance of 42.5 m, 47.3 m, and 38.3 m. For the latter stations,
 266 no data is available from 10 June, which does not hinder a comparison since the erup-
 267 tive pattern does not change with time (Eibl, Müller, et al., 2020). The data used are
 268 recorded on 3 June 2018 using a sampling rate of 200 Hz.

269 Based on the same seismic dataset, Eibl et al. (2021) suggested that the conduit
 270 is linked to a horizontal crack and a bubble reservoir at 23.7 ± 4.4 m depth, where the
 271 bubble reservoir extends from about 13 to 23 m west of the conduit and feeds eruptions
 272 of Strokkur. Strokkur passes through 4 phases during an eruptive cycle as laid out by
 273 Eibl et al. (2021) based on a multidisciplinary experiment (Eibl, Müller, et al., 2020).
 274 The illustration of the phases is shown in Fig. 3a).

275 The cycle starts with Phase 1 (P1), when an eruption is confirmed visually: a ris-
 276 ing bubble slug reaches the surface, bursts, and pushes the water and steam upwards into
 277 a jetting water fountain. P1 ends when the eruption stops. Due to the water loss in the
 278 conduit, the water from the pool and water from a shallow aquifer flow back to refill the
 279 conduit. This process is identified as Phase 2 (P2). At the beginning of Phase 3 (P3),
 280 the water temperature in the bubble reservoir is low due to the heat loss during the erup-
 281 tion. Seismically, this phase features an eruption coda interpreted as steam entering the
 282 reservoir, which partly collapses (Eibl et al., 2021). The collapses release heat and there-
 283 fore increase the temperature of the water in the bubble reservoir, eventually support-
 284 ing the gas accumulation toward the end of P3. In Phase 4 (P4), bubbles regularly leave

285 the bubble reservoir, migrate through the horizontal crack, and collapse at a temporal
 286 spacing of 21 to 26 s when reaching the water in the conduit that is not hot enough to
 287 preserve the steam bubble. With the water in the conduit heating up, the system even-
 288 tually reaches conditions where steam bubbles burst on the surface, and the next erup-
 289 tion starts (P1).

290 4 Seismic Preprocessing and PE Setting at Strokkur

291 Previous volcano-seismic studies (Glynn & Konstantinou, 2016; Melchor et al., 2020)
 292 used only the vertical component of seismic data to calculate PE. We compared PE us-
 293 ing the vertical and both horizontal components (Fig. S2) of the stations S1, S2, S3, S4,
 294 and S5. While the PE trends of the three components are generally the same, the ver-
 295 tical component exhibits larger variations in PE. We also checked and compared the seis-
 296 mogram and the spectrogram of the three components. The vertical components of these
 297 5 stations display the largest amplitude. Therefore, we used the vertical components for
 298 the following analysis. Station G3 and G4 recorded larger amplitudes on the horizon-
 299 tal components while G2 on the vertical component. The seismic data were detrended,
 300 tapered, and instrument corrected to velocity. Afterward, a high pass Butterworth fil-
 301 ter of order 4 with a corner frequency of 1 Hz was applied to remove the oceanic micro-
 302 seism.

303 Based on the eruption catalog compiled by Eibl et al. (2019), there were 63 erup-
 304 tions recorded on 10 June 2018 from midnight to 04:17 in the morning. These eruptions
 305 consisted of 53 single eruptions, 8 double eruptions, one triple eruption, and one quadru-
 306 ple eruption. As the waiting times after eruptions are in the order of minutes, and changes
 307 within the cycle occur within less than a second (Eibl et al., 2021), we aim for PE with
 308 high temporal resolution. In that case, we need to find the shortest window length pos-
 309 sible to calculate PE. We chose a window length of 1 s as it provides a good temporal
 310 resolution. The window length needs to contain more samples than the maximum pos-
 311 sible $m!$ ordinal patterns constructed from the embedding dimension m . In this case, the
 312 highest embedding dimension that can be applied for a 1 s window length with a sam-
 313 pling frequency of 400 Hz is 5.

314 Since the stations are a few meters from the place where the bubbles burst (Fig. 1),
 315 the signal-to-noise ratio is high. According to our synthetic test of signals without noise
 316 in Fig. 2a, the minimum PE is obtained using the shortest delay time. To confirm this
 317 in the real seismic data, we compare five different estimations using small delay times,
 318 ranging from 0.0025 s to 0.0125 s (Fig. S3). The PE variations related to these five dif-
 319 ferent delay times exhibit consistent patterns, with a difference in the absolute values.
 320 As we are only interested in relative PE changes during the eruptive cycle and not in its
 321 absolute values, it is safe to use one of them. In this paper, we present the result of PE
 322 using a delay time of 0.005 s.

323 In addition to PE, we calculated the Root-Mean-Square (RMS) of the ground mo-
 324 tion in velocity using the same 1 s long time window. Both quantities will be further eval-
 325 uated for their performance in eruption forecasting.

326 5 Results

327 5.1 PE and RMS Variation during an Eruptive Cycle

328 Repetitive patterns of the eruptive cycle for 63 eruptions recorded on 10 June 2018
 329 are visible in seismogram, spectrogram, RMS, and PE. An exemplary single eruption start-
 330 ing at 00:24:39 recorded at station S1 is shown in Fig. 3b-e.

331 The RMS rises at the beginning of P1 and drops at the end of P1 (Fig. 3d). It stays
 332 low during P2 but increases again when P3 starts. In P3, RMS shows a so-called erup-

333 tion coda composed of seismic peaks at a temporal spacing of 1.5 to 1.7 s featuring a fast
 334 increase and a slow decrease in amplitude. The RMS features regular peaks during P4
 335 at an average temporal spacing of 22 to 27 s. Each of these peaks is followed by a weak
 336 eruption coda, while the seismic amplitude of the peaks tends to decrease towards the
 337 end of P4 (Eibl et al., 2021). The last peak is not followed by an eruption coda.

338 Fig. 3e exhibits a high PE of 0.89 at the beginning of P1, then increases to the max-
 339 imum value of 0.94. PE slightly decreases at the start of P2 and suddenly drops towards
 340 P3. In P3, PE reaches a minimum value of 0.57, followed by a gradual increase towards
 341 P4. At the start of P4, PE reaches a value of 0.81 and sharply drops to 0.60. The fol-
 342 lowing trend then repeats several times: The PE gradually increases to about 0.83 and
 343 sharply decreases to about 0.61. In the last 12 s of P4, PE reaches a value of 0.80 and
 344 remains high before it increases further and the next eruption (P1) starts. The double,
 345 triple, and quadruple eruptions also show similar patterns.

346 5.2 Stacked PE, RMS, and Hypocentral Distances of 53 Single Erup- 347 tions

348 To assess the repetitive pattern of PE and RMS, we stacked the PE and RMS of
 349 the 53 cycles, started with a single eruption, according to the start time of each phase.
 350 For better visualization, we calculated the mean and the 68% confidence interval (writ-
 351 ten as mean [lower bound, upper bound]) using a 1 s window. The 68% confidence in-
 352 terval is equivalent to plus/minus one standard deviation for a Gaussian distribution.
 353 If the pattern of PE and RMS in each phase is similar from one eruption to another erup-
 354 tion, stacking them will reduce the noise and enhance the pattern.

355 We aligned the RMS from 55 s before to 50 s after the onset of each phase (Fig. 4a-
 356 d). The stacked RMS on each phase shows a clear pattern. At 35 s and 15 s before the
 357 onset of P1, two seismic peaks reach the mean RMS of $8.2 \cdot 10^{-7}$ m/s and $9.4 \cdot 10^{-7}$
 358 m/s, respectively. While both peaks are followed by a decrease in seismic amplitude, the
 359 second last peak is also followed by a weak eruption coda (Fig. 4a). At the onset of P1,
 360 the seismic amplitude increases toward the peak at the mean velocity of $7.9 [3.4, 11] \cdot 10^{-6}$ m/s
 361 (Fig. 4a). It drops rapidly to the onset of P2 (Fig. 4b). At the onset of P3, the seismic
 362 amplitude increases fast to the mean velocity of $1.2 [0.5, 1.9] \cdot 10^{-6}$ m/s and slowly de-
 363 creases towards the end of the phase (Fig. 4c). P4 starts with a sudden peak of mean
 364 velocity with a value of $6.7 [3.8, 9.9] \cdot 10^{-6}$ m/s followed by a weak eruption coda (Fig. 4d).

365 The stacked PE shows a stable pattern during the different eruptive cycles with
 366 different behavior than RMS. Around 35 s before the eruption, we see the last peak reach-
 367 ing a value of 0.78 [0.72, 0.83] in P4. Then the PE value drops to 0.68 [0.59, 0.76] about
 368 27 s before the eruption. Around 15 s before the eruption, the mean of PE reaches a sim-
 369 ilar value as the last peak of P4. However, instead of decreasing like after the previous
 370 peaks, PE remains high for about 6 s and then increases for 8 s to 0.90 [0.88, 0.93] at the
 371 start of P1 (Fig. 4e). The PE decreases slightly to P2 and drops to 0.70 [0.61, 0.78] at
 372 the beginning of P3 (Fig. 4f-g). PE continues declining for around 3 s to the minimum
 373 PE of 0.63 [0.57, 0.68]. After reaching the minimum, PE increases gradually for about
 374 31 s to 0.80 [0.77, 0.82] at the onset of P4 (Fig. 4h). PE then rapidly decreases to 0.63
 375 [0.59, 0.80] for about 8 s after the peak. This pattern repeats several times in P4 before
 376 the pattern changes about 14 s before P1.

377 To investigate the relation between PE and the distance to the source, we calcu-
 378 lated the distances from the estimated median source locations (Eibl et al., 2021) to the
 379 station S1. S1 is located about 10 m to the south of the conduit on the surface. Eibl et
 380 al. (2021) estimated the source location by using the particle motion of the recorded seis-
 381 mic waves. The epicenters of the sources were estimated from the intersection of the az-
 382 imuth angles derived from all 5 stations. Eibl et al. (2021) project the epicenter loca-
 383 tion vertically down and extract the source depth from the intersection point with the

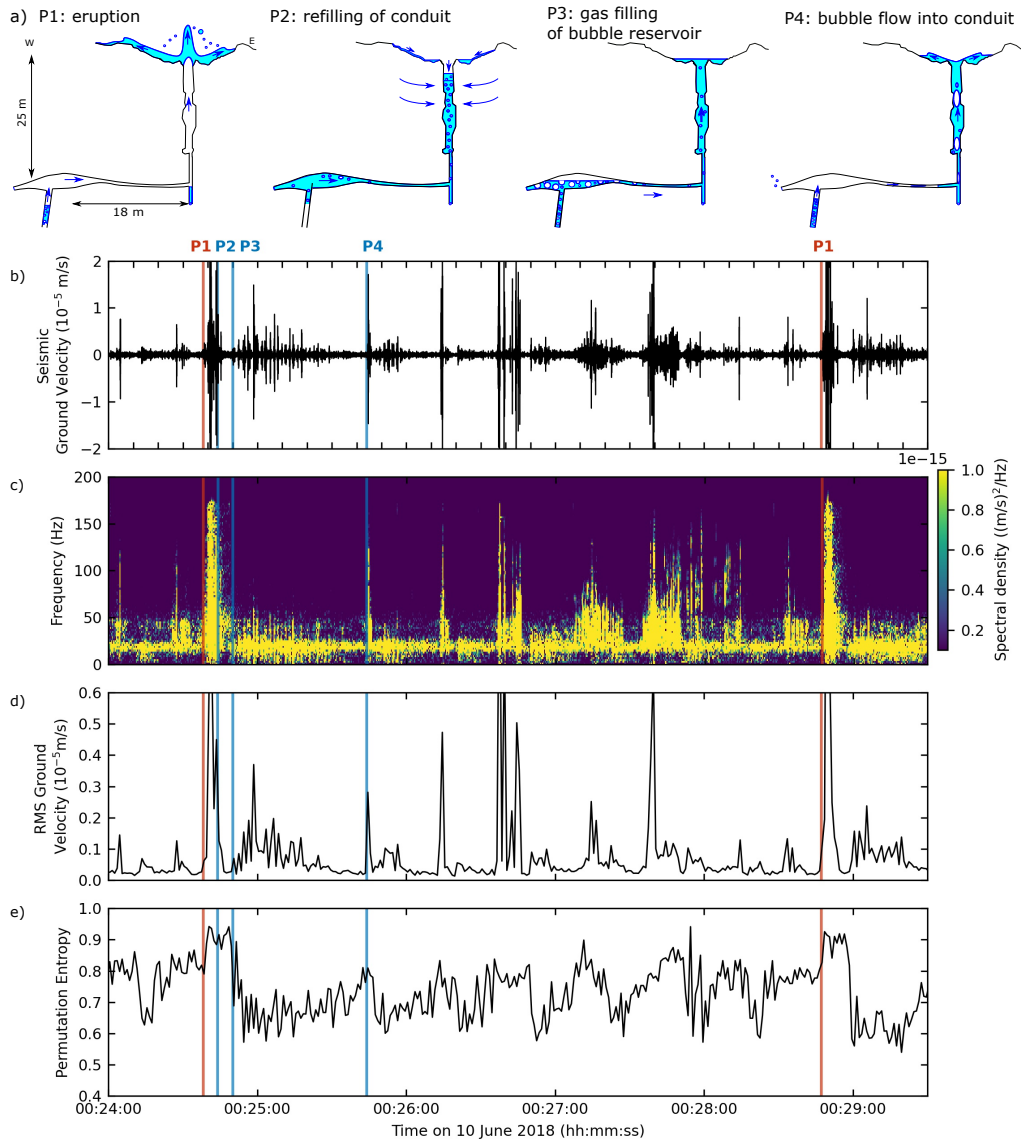


Figure 3. A typical eruptive cycle of a single eruption recorded on 10 June 2018. (a) Illustration of the phases of the eruptive cycle at Strokkur modified from Eibl et al. (2021), (b) Seismogram of the vertical component after high pass filtering with a corner frequency of 1 Hz. The two vertical red lines refer to the start of P1, while the blue lines refer to the start of P2, P3, and P4 as illustrated in subfigure (a), (c) Amplitude Spectrogram of subfigure (b) using a time window of 256 samples and overlap of 50 samples, (d) RMS and (e) PE calculated in non-overlapping 1 s long time windows for the seismic data shown in subfigure (b).

384 derived incidence angles for all stations. Note that the shallow source depths during P1
 385 and peaks in P4 are poorly constrained since the particle motion shows an elliptical par-
 386 ticle motion characteristic for Rayleigh waves when the seismic sources reach or approach
 387 the surface. We stacked the hypocentral distances from the sources to S1 and calculated
 388 their mean and the confidence interval (Fig. 4i-l).

389 We notice that from 15 s before the eruption, the seismic sources remain at about
 390 10 m depth from the surface or about 20 m away from S1 until the eruption occurs (Fig. 4i).

391 The source gradually deepens in P2 and reaches a distance of 34 m from S1 (Fig. 4j-k).
 392 The sources in P3 are mostly located 13 to 23 m west of the conduit (Eibl et al., 2021),
 393 then hypocentral distances decrease toward P4. We checked the source depth and ob-
 394 served that the seismic sources migrate upwards towards the start of P4. P4 starts with
 395 seismic sources at a depth of about 10 m with a distance of 21 m to S1. It is likely that
 396 the seismic source reached less than 10 m depths during the peaks in P4 (Fig. 4l) and
 397 even more during P1, when the eruption occurs on the surface (Fig. 4i).

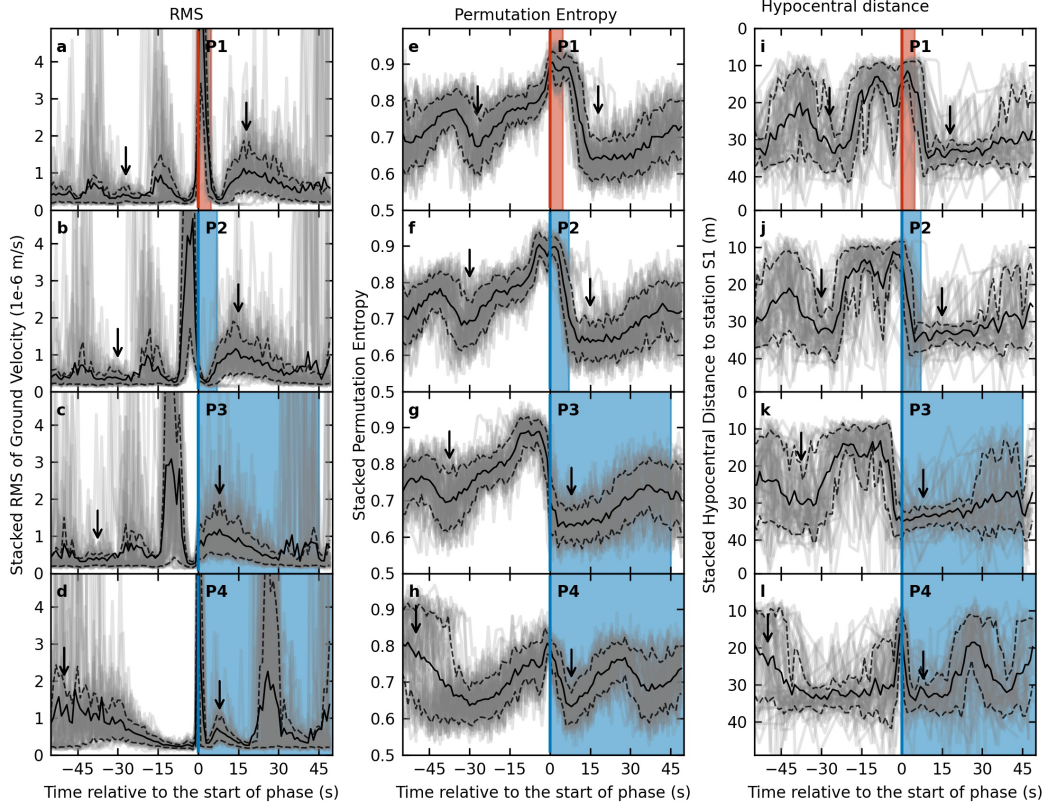


Figure 4. Stacked RMS, PE, and hypocentral distance values for the 53 cycles of single eruptions recorded at station S1. Grey lines mark the RMS values for each eruption aligned at (a) the start of the eruption (P1), (b) the end of the eruption (start of P2), (c) the start of the eruption coda (P3), and (d) the start of P4 with regular bubble collapses in the conduit at depth. The time is measured relative to the alignment time (i.e., the start of the red or blue area highlighting the mean duration of the phase). The black lines define the mean values in a 1 s window, while the dashed lines represent the 68% confidence interval. The black arrows point to the seismic eruption coda visible in P3 and P4. (e-l) Same as subfigures (a-d) for (e-h) PE and (i-l) the distance between the seismic source location and station S1 (Eibl et al., 2021).

398 5.3 PE Pattern with Respect to Double to Quadruple Eruptions

399 We also assessed the PE pattern of 8 double eruptions recorded on 10 June 2018.
 400 These eruptions consist of two water fountains at an average temporal spacing of 15.6 s,
 401 and the duration of phases P3 and P4 increase linearly with respect to single eruptions
 402 (Eibl et al., 2021). The PE pattern of double eruptions throughout the cycle is similar

403 to single eruptions. Its variation is not systematically higher or lower than for single erup-
 404 tions. While in single eruptions, the PE drastically drops, on average, after 8 s from the
 405 beginning of the eruptions, the PE of double eruptions remains high until the second wa-
 406 ter fountain. PE only drops when entering P3 on average 28 s after the beginning of the
 407 first water fountain (Fig. S4).

408 There was only one triple and one quadruple eruption during the whole recording
 409 period. In general, the PE patterns for both triple and quadruple are similar to the sin-
 410 gles and double eruptions, with PE remaining high in P1 until the last water fountain oc-
 411 curred.

412 5.4 Reliability of PE Results with Respect to Distance from the Source

413 To evaluate the performance of PE with respect to the station location, we com-
 414 pared the stacked PE variations obtained for the records at stations S1, S2, S3, S4, and
 415 S5. We also calculated the variations of the stacked source-station distance for the same
 416 stations in the same way. Supplementary Fig. S5 shows that PE is sensitive with respect
 417 to the stations' locations. The differences in source distance to each station are small,
 418 but the absolute values of PE for different stations are quite distinct. S1, which is lo-
 419 cated closest to the seismic sources, exhibits the lowest absolute values of PE compared
 420 to the other stations. S2, S3, and S4 display a similar temporal variation as S1 but with
 421 higher absolute values throughout the cycles. An exception is station S5. While the dis-
 422 tance from S5 to the seismic sources is similar to the other stations, the temporal vari-
 423 ation of PE does not reflect clearly the changing phases in the eruptive cycle. Overall,
 424 the PE at station S5 is dominated by high values except for the first half of P3. The PE
 425 in P4 is as high as in P1, making it difficult to see the transition to the eruption in the
 426 PE value.

427 To investigate further the performance of PE at stations with a larger distance, we
 428 calculated PE of seismic data recorded at stations G2, G3, and G4 (Fig. 1b) on 3 June
 429 2018. These three stations are located at 42.5 m, 47.3 m, and 38.3 m north-west, west,
 430 and south-east of the conduit, respectively. PE values at G2 and G4 are mostly confined
 431 between 0.8 and 0.9 and exhibit more random patterns which do not correlate with the
 432 eruption phase (see Fig. S6.a and c). However at G3, PE behaves similarly to PE at S1
 433 to S5, even though it is in a lower range and there is no clear transition toward erup-
 434 tions (see Fig. S6.b).

435 6 Interpretation and Discussion

436 6.1 PE extracting the dynamical information from seismic wave

437 PE does not depend on the absolute amplitudes, and multiplying a signal by a fac-
 438 tor leads to the same PE value. In contrast, PE depends on the frequency bandwidth
 439 of the signal. Our synthetic test shows that a synthetic signal containing more frequen-
 440 cies, i.e., by superposing more harmonic signals, produces a higher PE than a signal con-
 441 taining fewer frequencies. We suggest that a signal with a broader frequency content has
 442 a higher PE compared to a signal with a narrower frequency band. Dávalos et al. (2021)
 443 investigated the effect of bandpass filters such as Butterworth and Chebyshev applied
 444 before the PE calculation and observed that lower PE corresponded to narrower band-
 445 widths while higher PE corresponded to broader bandwidths. Our synthetic tests con-
 446 firm their result.

447 Our observation at Strokkur shows that PE reaches the highest value during the
 448 eruption phase (P1) when the water jets into the air. In this phase, the amplitude peaks
 449 and the frequency content is broad. Once the last fountain stops (P2), the amplitude quickly
 450 drops and declines to narrower bandwidth. PE is still high at the end of the last foun-

tain but then quickly drops to the next phase (P3). During P3, the eruption coda is composed of seismic peaks at a temporal spacing of 1.5 to 1.7 s. Whilst their frequency content is broad, it is not as broad as during seismic peaks in P1 and P4. Between these peaks in P3, the frequency content of the seismic signal is narrow banded, and the PE fluctuates and reaches minimum values. In P4, during the regular peaks and broad spectrum of the energy produced by the bubble collapses at depth, PE reaches the local maximum. Conversely, PE is smallest directly after the peaks in P4 despite a starting eruption coda that increases in amplitude and widens in frequency content. Shortly before the next peak in P4, it seems seismically quiet and with a narrow-banded frequency content, while the PE value keeps increasing. The PE hence does not solely depend on the broadness of the frequency spectrum.

During P4, the two last bubble collapses at depth in the conduit happen about 35 and 15 s before the start of the next eruption, respectively. Both collapses are recorded as a peak in seismic amplitude and are followed by a drop in seismic amplitude, as seen in the stacked RMS. During these collapses, the PE values reach a local maximum. Following the second last collapse, the PE value drops, while it remains high after the last bubble collapse. We further investigated the waveforms and spectrograms in the last 50 s before the eruption. The second last collapse is followed by a weak eruption coda. This coda is similar to the eruption coda in P3 in terms of the peaks' temporal spacing and frequency content. However, it is smaller in amplitude, and the duration is shorter than in P3. In contrast, the last collapse before the eruption is not followed by an eruption coda. Hence, the RMS value drops to a lower amplitude while the PE value remains high. With respect to the state of the geyser, this implies that the second last bubble collapse triggers recharge in the reservoir, while after the last bubble collapse at depth, the system has reached a state that is ready for eruption. At that stage, the water in the reservoir and conduit is most likely heated sufficiently - without further need to recharge - and contains small bubbles in the whole pipe system. The next large bubble that rises in the conduit can then reach the surface and burst into a jetting water fountain.

Eibl et al. (2021) observed a decrease in seismic peak amplitude during collapses in the conduit with time. They speculate that this is due to damping when more bubbles accumulate in the conduit and decouple the noise from the bubbles and the conduit walls. Here, an increasing amount of bubbles might then suggest that the PE values throughout P4 should increase. While in some eruptions, such a linear increase trend can be observed throughout P4, it is not always the case.

Glynn and Konstantinou (2016) observed an increase of PE for two days between a 5.6 Mw earthquake in Bárðarbunga on 29 September 1996 and the onset of a subglacial eruption in Gjálp on 1 October 1996. This PE increase was preceded by 8 days of PE decrease, which they associated with the lack of frequencies higher than 1 Hz. After the 5.6 Mw earthquake, earthquake swarms migrated to the Gjálp fissures featuring broader frequencies in the range of 0.1 to 9 Hz at station HOT23, located at 8 km distance (Konstantinou et al., 2020). Glynn and Konstantinou (2016) suggested that these higher frequencies increase the complexity, hence causing the PE to increase.

We tested the performance of PE using acceleration derived from the ground velocity and also find an increase in PE. Differentiating velocity into acceleration enhances the energy at higher frequencies. However, we found that the PE values obtained from acceleration are not only larger than PE obtained from velocity but also more confined to a narrower range featuring less variation throughout the eruptive cycle. An example is given in Fig. S7 for PE calculated using $m = 5$ and $\tau = 0.005$ s at station S1.

There are two possible reasons why PE obtained from acceleration is less sensitive toward the process inside the geyser than from velocity. First, acceleration enhances the part of the high-frequency signal which is susceptible to the scattering effect from the lateral heterogeneity of the upper crust. This path effect could blur the information of

503 the source mechanism carried by the signal. Second, resolving the complexity of broader
 504 spectra requires a higher embedding dimension. In the case of Strokkur, as we aim for
 505 1 s resolution and given the sampling frequency of 400 Hz, the highest embedding di-
 506 mension (m) which we can use is 5.

507 **6.2 The influence of source strength and path effects toward the PE per-** 508 **formance**

509 We observed that the PE at stations S1, S2, S3, and S4 correlates strongly with
 510 the distance between seismic sources and the station. As the seismic sources migrate to
 511 the surface and the source-station distance decreases PE increases. First, it should be
 512 considered that each phase in the eruptive cycle, which occurs at different depth inter-
 513 vals, is associated with different physical processes (see 3a). Those physical processes might
 514 be associated with different PE values. Second, high frequencies are attenuated with dis-
 515 tance. If the attenuation eliminates energy and causes the frequency band to become nar-
 516 rower, PE will decrease. However, PE at station S5 exhibits high PE values and less change
 517 throughout all phases. Possible reasons are discussed in the following.

518 The seismic sources, mostly located at average depths of 23.7 ± 4.4 m and $9.9 \pm$
 519 4.1 m (Eibl et al., 2021), are subject to the strong attenuation due to the lateral and ver-
 520 tical heterogeneity in Iceland’s upper crust (Foulger et al., 2003; Menke et al., 1995). Sato
 521 and Fehler (1998) suggested that the particle motion of the P-wave should be linearly
 522 polarized if it travels through a path with no or small scattering. When P-wave parti-
 523 cle motion is elliptical or even spherical, it indicates strong scattering. Eibl et al. (2021)
 524 observed linear particle motions at stations S1 to S4, while station S5 exhibits low lin-
 525 earity. This could suggest that the seismic waves arriving at S5 are much more scattered
 526 compared to the other four stations. Scattering attenuation could increase the complex-
 527 ity of the seismic waves due to the superposition between waves in a heterogeneous medium
 528 and lead to a more uniform frequency distribution, hence increasing PE.

529 At larger distances of 38.3 to 47.3 m, the PE performance deteriorates. When the
 530 seismic source only releases a small amount of energy, and the distance of the source to
 531 the station is large, PE seems to reflect more the filtering of the seismic wave during its
 532 propagation to the station. This is also supported by the findings of Eibl et al. (2021),
 533 who could not use these stations for the seismic source location due to low-quality par-
 534 ticle motions. By contrast, the drop of PE prior to the 5.6 Mw earthquake at Bárðar-
 535 bunga two days before the 1996 Gjálp eruption, could be detected by stations at a 100
 536 km distance (Glynn & Konstantinou, 2016). This drop is thought to be caused by in-
 537 trinsic attenuation when hot magma ascended to the upper crust. If the depth of the magma
 538 chamber feeding the eruption is estimated to be between 8 and 12 km (Konstantinou et
 539 al., 2020), then the seismic sources are located at depths between mid to upper crust.
 540 The attenuation at this depth is much lower compared to the uppermost 4 km of crust
 541 (Menke et al., 1995). Moreover, the pressurization of magma triggered the 5.6 Mw earth-
 542 quake. The differences in the source strength and the path effect could explain the per-
 543 formance differences between PE at Strokkur and Bárðarbunga.

544 **6.3 Predictive power of PE in comparison to RMS**

545 We used the ROC analysis to quantify the predictive power of PE in comparison
 546 to RMS. The resulting curves are shown in Fig. 5 for alarms raised for the next time step
 547 when the variables exceed a certain threshold. PE demonstrates good predictive skills
 548 with $AUC=0.846$, while RMS is even worse than random with $AUC=0.433$. The latter
 549 is not surprising, having in mind that RMS tends to decrease prior to eruptions (see Fig. 4a).
 550 Thus, we also calculated the inverse of RMS as a measure of quiescence. However, $1/RMS$
 551 yields $AUC=0.567$ which is only slightly better than a random forecast.

552 To rank the predictive power of the PE using only 1 s bin information, we also ap-
 553 plied the statistical recurrence model of Eibl, Hainzl, et al. (2020) which was inferred from
 554 20390 waiting times after eruptions of Strokkur geyser in December 2017 and January
 555 2018. The analysis of this long sequence revealed log-normal recurrences with mean and
 556 standard deviations dependent on the eruption type of the last event. In particular, we
 557 determined the probability p_T of the next event within the alarm time, knowing the time
 558 to the last eruption and its eruption style. A detailed description of the calculation of
 559 these probabilities is provided in the Appendix. This probability value is found to out-
 560 perform PE with AUC=0.971. Of course, the comparison is unfair because p_T is based
 561 on combined information over a very long time. However, PE can even improve the p_T -
 562 result if the product of both variables is considered. This result can be understood by
 563 considering that p_T is monotonously increasing with increasing time to the last eruption.
 564 At the same time, PE is similarly high at intermediate bubble collapses at depth as be-
 565 fore the eruptions (see Fig. 3e). The multiplication (shown in the black dashed and con-
 566 tinuous lines in Fig. 5) suppresses the high values related to bubble collapses, leading
 567 to an enhanced forecast power. This effect is amplified, if the mean ($\langle PE \rangle$) value is re-
 568 moved from the PE signal, $PE_n = (PE - \langle PE \rangle) H(PE - \langle PE \rangle)$, with H the Heaviside func-
 569 tion (H(x)=1 if x>0 and zero else). In this case, the AUC is 0.99, very close to the op-
 570 timal value of 1.0.

571 Note that to test the predictive power of PE and RMS, we have only used so far
 572 the information in separate 1 s bins of the seismogram. We ignored the information en-
 573 coded in the time evolution of these parameters. Analyzing the possible improvements
 574 using the full PE and RMS patterns requires machine learning techniques and is left for
 future studies.

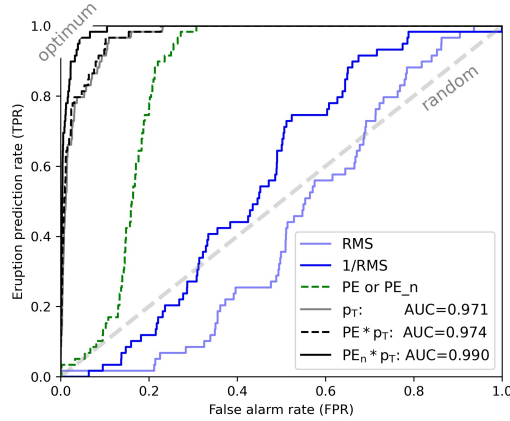


Figure 5. Assessing the predictive power of PE using ROC. ROC curves for PE and PE_n (dashed green, note that the PE and PE_n curves are identical), RMS (light blue), the inverse of RMS (blue), and the probability p_T calculated for the recurrence model of Eibl, Hainzl, et al. (2020) (grey), as well as combinations of the latter with PE (solid black and dashed black). Here, PE_n refers to the rescaled PE value, $PE_n = (PE - \langle PE \rangle) H(PE - \langle PE \rangle)$, with $\langle PE \rangle$ being the mean value of PE and H the Heaviside function. The alarm period is the next time step ($N_T=1$) with the corresponding AUC values given in the legend. The result of a random variable is indicated by the dashed diagonal with AUC=0.5, while the result of an optimal predictor is marked in the upper left corner.

575

576 7 Conclusions

577 In this research, we show a good capability of PE in characterizing different phases
 578 in the eruptive cycle of the Strokkur geyser. PE also performs better in predicting an
 579 eruption than RMS of the ground velocity. About 15 s before the eruption, PE indicates
 580 that the system is prone to erupt after the last collapse by increasing values. At the same
 581 time, the RMS indicates quiescence, and the seismic sources remain at a shallow depth.
 582 The PE reflects the seismic changes linked to a state with superheated water in the pipe
 583 system and small bubbles drifting in it. Hence, the PE might be indirectly sensitive to
 584 the number of small bubbles present in the water.

585 PE can characterize the different phases of the geyser’s eruptive cycle for the near-
 586 field stations, but it seems that PE cannot resolve the dynamics for signals at larger dis-
 587 tances. Depending on the signal strength at the source and the signal-to-noise ratio, our
 588 results indicate that this method requires seismic data recorded as close to the source
 589 as possible, in the case of Strokkur within 15 m. Defining suitable preprocessing steps
 590 for PE application on a volcano requires further research. While in a geyser, the inter-
 591 action between the water and gas with the surrounding rock mostly generates tremors,
 592 the interaction between magma and the surrounding rock in a volcano generates more
 593 types of volcano-seismic signals with different complexities. For monitoring a volcano,
 594 the seismic stations are usually installed at larger distances, which will decrease the sig-
 595 nal strength. These factors need to be taken into account. Nonetheless, PE has a strong
 596 potential to contribute to the framework of eruption forecasting. For this purpose, our
 597 study might help to define distinct precursory features in the temporal variation of PE
 598 prior to eruptions that are useful for eruption forecasting.

599 Appendix A Eruption probabilities based on the recurrence model of 600 Eibl, Hainzl, et al. (2020)

601 We calculated the eruption probability for 1 s alarm times using the statistical model
 602 of Eibl, Hainzl, et al. (2020). The analysis of 20390 eruptions between December 2017
 603 and January 2018 revealed a log-normal distribution $f_x(t)$ as the probability density func-
 604 tion of the inter-eruption times t at Strokkur, where the parameters depend on the type
 605 x (single, double, triple, quadruple) of the last eruption. In particular, the mean ($\langle t \rangle$)
 606 and standard deviation (σ_t) of the inter-eruption times are $\langle t \rangle=3.8$, $\sigma_t=0.8$ ($x=1$), $\langle t \rangle=6.6$,
 607 $\sigma_t=1.7$ ($x=2$), $\langle t \rangle=9.5$, $\sigma_t=2.5$ ($x=3$), $\langle t \rangle=12.4$, $\sigma_t=3.4$ ($x=4$), $\langle t \rangle=15.2$, $\sigma_t=4.1$ ($x=5$),
 608 and $\langle t \rangle=17.7$, $\sigma_t=4.5$ ($x=6$).

609 Based on those log-normal distributions and knowing the actual waiting time (t_w)
 610 since the last eruption and its style (x), the probability (p) for an eruption in the period
 611 $[t_1, t_1 + T]$ (with $t_1 \geq t_w$) is calculated according to

$$612 \quad p_x([t_1, t_1 + T]|t_w) = \frac{\int_{t_1}^{t_1+T} f_x(t) dt}{\int_{t_w}^{\infty} f_x(t) dt} \quad (\text{A1})$$

613 Note that the denominator is the survival function of $f_x(t)$ for given t_w , which is nec-
 614 essary to normalize the distribution for $[t_w, \infty]$.

615 Open Research

616 The seismic data used in this paper are available through GEOFON (Eibl, Wal-
 617 ter, et al., 2020) via <https://geofon.gfz-potsdam.de/doi/network/7L/2017>. The scripts
 618 to calculate PE are available at <https://gitup.uni-potsdam.de/pujiastutisudiby/permutationentropy>.

619 Acknowledgments

620 We thank the Environment Agency of Iceland and the National Energy Authority for
 621 the research permit around Strokkur in the Geysir geothermal area. We thank the rangers
 622 and Daniel Vollmer for support and guidance in the field. This work was financially sup-
 623 ported by DAAD under grant 57507871. We would like to thank Satoshi Ide, Kostas Kon-
 624 stantinou, and the anonymous associate editor and first reviewer for their constructive
 625 reviews that helped improving this manuscript. We declared that this work does not con-
 626 tain any conflict of interests.

627 References

- 628 Bandt, C., & Pompe, B. (2002). Permutation entropy: A natural complexity
 629 measure for time series. *Physical Review Letters*, *73*(17). doi: 10.1103/
 630 PhysRevLett.88.174102
- 631 Bell, A. F., Naylor, M., & Main, I. G. (2013, 06). The limits of predictability of
 632 volcanic eruptions from accelerating rates of earthquakes. *Geophysical Journal*
 633 *International*, *194*(3), 1541-1553. Retrieved from [https://doi.org/10.1093/
 634 gji/ggt191](https://doi.org/10.1093/gji/ggt191) doi: 10.1093/gji/ggt191
- 635 Boué, A., Cortés, G., Vallete, B., & G, R. (2015). Real-time eruption forecasting us-
 636 ing the material failure forecast method with a bayesian approach. *Journal of*
 637 *Geophysical Research: Solid Earth*, *120*. doi: 10.1002/2014JB011637
- 638 Cao, Y., Tung, W.-w., Gao, J. B., Protopopescu, V. A., & Hively, L. M. (2004).
 639 Detecting dynamical changes in time series using permutation entropy.
 640 *Physical review. E, Statistical, nonlinear, and soft matter physics*, *70*. doi:
 641 10.1103/PhysRevE.70.046217
- 642 Cánovas, J. S., Guillamón, A., & Ruiz, M. C. (2011). Using permutations to find the
 643 structural changes in time series. *Fluctuation and Noise Letters*, *10*(1). doi: 10
 644 .1142/S0219477511000375
- 645 Dempsey, D. E., Cronin, S. J., Mei, S., & A.W, K. (2020). Automatic pre-
 646 cursor recognition and real-time forecasting of sudden explosive volcanic
 647 eruptions at whakaari, new zealand. *Nature Communication*, *11*. doi:
 648 1038/s41467-020-17375-2
- 649 DeVries, P. M. R., Viégas, F., Wattenberg, M., & Meade, B. J. (2018). Deep learn-
 650 ing of aftershock patterns following large earthquakes. *Nature*, *560*(7720), 632-
 651 634.
- 652 Dávalos, A., Jabloun, M., Ravier, P., & Buttelli, O. (2021). The impact of linear
 653 filter preprocessing in the interpretation of permutation entropy. *Entropy*, *23*.
 654 doi: 10.3390/e23070787
- 655 Eibl, E. P. S., Hainzl, S., Vesely, N. I. K., Walter, T. R., Jousset, P., Hersir, G. P., &
 656 Dahm, T. (2020). Eruption interval monitoring at Strokkur Geysir, Iceland.
 657 *Geophysical Research Letters*, *47*, e2019GL085266.
- 658 Eibl, E. P. S., Jousset, P., Dahm, T., Walter, T. R., Hersir, G. P., & Vesely,
 659 N. I. K. (2019). Seismic experiment at the strokkur geysir, iceland, allows
 660 to derive a catalogue of over 70,000 eruptions. *GFZ Data Services*. doi:
 661 <https://doi.org/10.5880/GFZ.2.1.2019.005>
- 662 Eibl, E. P. S., Müller, D., Allahbakhshi, M., Walter, T. R., Jousset, P., Hersir, G. P.,
 663 & Dahm, T. (2020). *Multidisciplinary dataset at the strokkur geysir, ice-
 664 land, allows to study internal processes and to image a bubble trap*. doi:
 665 10.5880/GFZ.2.1.2020.007
- 666 Eibl, E. P. S., Müller, D., Walter, T. R., Allahbakhshi, M., Jousset, P., Hersir,
 667 G. P., & Dahm, T. (2021). Eruptive cycle and bubble trap of Strokkur
 668 Geysir, Iceland. *Journal of Geophysical Research: Solid Earth*, *126*. doi:
 669 10.1029/2020JB020769
- 670 Eibl, E. P. S., Walter, T., Jousset, P., Dahm, T., Allahbakhshi, D., M.and Müller,
 671 & Hersir, G. (2020). 1 year seismological experiment at strokkur in 2017/18.

- 672 *GFZ Data Services. Other/Seismic Network*. doi: 10.14470/2Y7562610816
- 673 Endo, E. T., & Murray, T. (1991). Real-time seismic amplitude measurement
674 (rsam): a volcano monitoring and prediction tool. *Bulletin of Volcanology*, *53*,
675 533-545. doi: 10.1007/BF00298154
- 676 Fawcett, T. (2006). An introduction to ROC analysis. *Pattern Recognition Letters*,
677 *27*(8), 861-874.
- 678 Foulger, G. R., Du, Z., & Julian, B. R. (2003, 11). Icelandic-type crust. *Geophysical*
679 *Journal International*, *155*(2), 567-590. Retrieved from [https://doi.org/10](https://doi.org/10.1046/j.1365-246X.2003.02056.x)
680 [.1046/j.1365-246X.2003.02056.x](https://doi.org/10.1046/j.1365-246X.2003.02056.x) doi: 10.1046/j.1365-246X.2003.02056.x
- 681 Glynn, C. C., & Konstantinou, K. I. (2016). Reduction of randomness in seismic
682 noise as a short-term precursor to a volcanic eruption. *Scientific Reports*, *6*(1),
683 37733. Retrieved from <http://www.nature.com/articles/srep37733> doi: 10
684 [.1038/srep37733](https://doi.org/10.1038/srep37733)
- 685 Harris, C. R., Millman, K. J., van der Walt, S. J., Gommers, R., Virtanen, P., Cour-
686 napeau, D., ... Oliphant, T. E. (2020, September). Array programming with
687 NumPy. *Nature*, *585*(7825), 357-362. Retrieved from [https://doi.org/](https://doi.org/10.1038/s41586-020-2649-2)
688 [10.1038/s41586-020-2649-2](https://doi.org/10.1038/s41586-020-2649-2) doi: 10.1038/s41586-020-2649-2
- 689 Hurwitz, S., & Manga, M. (2017). The fascinating and complex dynamics of geyser
690 eruptions. *Annual Review of Earth and Planetary Sciences*, *45*(1), 31-59. doi:
691 [10.1146/annurev-earth-063016-015605](https://doi.org/10.1146/annurev-earth-063016-015605)
- 692 Kang, H., Zhang, X., & Zhang, G. (2021). Phase permutation entropy: A com-
693 plexity measure for nonlinear time series incorporating phase information.
694 *Physica A: Statistical Mechanics and its Applications*, *568*, 125686. Re-
695 trieved from [https://www.sciencedirect.com/science/article/pii/](https://www.sciencedirect.com/science/article/pii/S0378437120309845)
696 [S0378437120309845](https://www.sciencedirect.com/science/article/pii/S0378437120309845) doi: <https://doi.org/10.1016/j.physa.2020.125686>
- 697 Konstantinou, K., Utami, I., & Giannopoulos, D. (2020). A reappraisal of seismic-
698 ity recorded during the 1996 gjálp eruption, iceland, in light of the 2014–2015
699 bárdarbunga–holuhraun lateral dike intrusion. *Pure and Applied Geophysics*,
700 *177*, 2579–2595. doi: 10.1007/s00024-019-02387-x
- 701 McNutt, S. R. (1996). Seismic monitoring and eruption forecasting of volcanoes: A
702 review of the state-of-the-art and case histories. In *Monitoring and mitigation*
703 *of volcano hazards* (pp. 99–146). Springer Berlin Heidelberg. doi: 10.1007/978
704 [-3-642-80087-0_3](https://doi.org/10.1007/978-3-642-80087-0_3)
- 705 Melchor, I., Almendros, J., Carniel, R., Konstantinou, K. I., Hantusch, M., &
706 Caselli, A. (2020). On data reduction methods for volcanic tremor char-
707 acterization: the 2012 eruption of copahue volcano, southern andes. *Earth,*
708 *Planets and Space*, *72*, 134. doi: 10.1186/s40623-020-01270-7
- 709 Menke, W., Levin, V., & Sethi, R. (1995, 07). Seismic attenuation in the crust
710 at the mid-Atlantic plate boundary in south-west Iceland. *Geophysical Journal*
711 *International*, *122*(1), 175-182. Retrieved from [https://doi.org/10.1111/j](https://doi.org/10.1111/j.1365-246X.1995.tb03545.x)
712 [.1365-246X.1995.tb03545.x](https://doi.org/10.1111/j.1365-246X.1995.tb03545.x) doi: 10.1111/j.1365-246X.1995.tb03545.x
- 713 Moran, S. C., Freymueller, J. T., LaHusen, R. G., McGee, K. A., Poland, M. P.,
714 Power, J. A., ... White, R. A. (2008). *Instrumentation recommendations for*
715 *volcano monitoring at u.s. volcanoes under the national volcano early warning*
716 *system* (Tech. Rep.). U.S. Geological Survey.
- 717 Moran, S. C., Newhall, C., & Roman, D. C. (2011). Failed magmatic eruptions: late-
718 stage cessation of magma ascent. *Bulletin of Volcanology*, *73*(2). doi: 10.1007/
719 [s00445-010-0444-x](https://doi.org/10.1007/s00445-010-0444-x)
- 720 Rényi, A. (1960). *On measures of entropy and information* (Vol. 1). Berkeley: Uni-
721 versity of California Press.
- 722 Riedl, M., Müller, A., & Wessel, N. (2013). Practical considerations of permuta-
723 tion entropy: A tutorial review. *The European Physical Journal Special Top-*
724 *ics*, *222*(2), 249–262. Retrieved from [http://link.springer.com/10.1140/](http://link.springer.com/10.1140/epjst/e2013-01862-7)
725 [epjst/e2013-01862-7](http://link.springer.com/10.1140/epjst/e2013-01862-7) doi: 10.1140/epjst/e2013-01862-7
- 726 Rinehart, J. S. (1986). Seismic signatures of some icelandic geysers. *Journal of Geo-*

- 727 *physical Research*, 73. doi: 10.1029/JB073i014p04609
- 728 Sato, H., & Fehler, M. C. (1998). *Seismic wave propagation and scattering in the*
729 *heterogeneous earth / haruo sato, michael c. fehler*. New York: AIP Press.
- 730 Spampinato, S., Langer, H., Messina, A., & Falsaperla, S. (2019). Short-term de-
731 tection of volcanic unrest at Mt. Etna by means of a multi-station warning
732 system. *Scientific Reports*, 9, 6506. doi: 10.1038/s41598-019-42930-3
- 733 Van Rossum, G., & Drake, F. L. (2009). *Python 3 reference manual*. Scotts Valley,
734 CA: CreateSpace.
- 735 Walter, T. R., Jousset, P., Allahbakhshi, M., Witt, T., Gudmundsson, M. T., &
736 Hersir, G. P. (2020). Underwater and drone based photogrammetry reveals
737 structural control at geysir geothermal field in iceland. *Journal of Volcanology*
738 *and Geothermal Research*, 391. doi: 10.1016/j.jvolgeores.2018.01.010
- 739 White, D. E. (1967). Some principles of geyser activity, mainly from steamboat
740 springs, nevada. *American Journal of Science*, 265(8), 641–684. Retrieved
741 from <https://www.ajsonline.org/content/265/8/641> doi: 10.2475/ajs.265
742 .8.641
- 743 Whitehead, M. G., & Bebbington, M. S. (2021). Method selection in short-term
744 eruption forecasting. *Journal of Volcanology and Geothermal Research*, 419.
745 doi: 10.1016/j.jvolgeores.2021.107386
- 746 Zanin, M., Zunino, L., Rosso, O. A., & David, P. (2012). Permutation entropy
747 and its main biomedical and econophysics applications: A review. *Entropy*, 14,
748 1553–1577. doi: 10.3390/e14081553
- 749 Zhao, X., Shang, P., & Huang, J. (2013, may). Permutation complexity and depen-
750 dence measures of time series. *EPL (Europhysics Letters)*, 102(4), 40005. Re-
751 trieved from <https://doi.org/10.1209/0295-5075/102/40005> doi: 10.1209/
752 0295-5075/102/40005
- 753 Zunino, L., Olivares, F., Scholkmann, F., & Rosso, O. A. (2017). Permuta-
754 tion entropy based time series analysis: Equalities in the input signal can
755 lead to false conclusions. *Physics Letters A*, 381(22), 1883–1892. doi:
756 10.1016/j.physleta.2017.03.052
- 757 Zunino, L., Pérez, D., Kowalski, A., Martín, M., Garavaglia, M., Plastino, A.,
758 & Rosso, O. (2008). Fractional brownian motion, fractional gaussian
759 noise, and tsallis permutation entropy. *Physica A: Statistical Mechan-*
760 *ics and its Applications*, 387(24), 6057–6068. Retrieved from [https://](https://www.sciencedirect.com/science/article/pii/S0378437108006043)
761 www.sciencedirect.com/science/article/pii/S0378437108006043 doi:
762 <https://doi.org/10.1016/j.physa.2008.07.004>